AIAA JOURNAL
Vol. 43, No. 2, February 2005

Reduced-Order Modeling of a Heaving Airfoil

G. C. Lewin* and H. Haj-Hariri†
University of Virginia, Charlottesville, Virginia 22904

A method for generating a reduced-order model of a flapping airfoil is presented. Using proper orthogonal decomposition, sets of orthogonal basis functions are generated from snapshots produced from previous computational (Navier–Stokes) results. With proper orthogonal decomposition, most of the energy in the flow is concentrated in just a few basis functions. These functions are used for a Galerkin projection of the Navier–Stokes equations, reducing them to a small set of coupled, nonlinear ordinary differential equations. The reduced-order model is used to simulate heaving motions that are both similar to and different from the motion(s) used to generate the basis functions, and the errors in the model are quantified. Several methods are used to generate mode sets that can be used over a range of heaving parameters, including snapshots from one, two, and multiple Navier–Stokes simulations. As snapshots from additional simulations are added to the decomposition, the mode sets become "richer" and can simulate a wider range of parameter space. This richness, however, requires retaining more modes in the reduced-order model, adding to the computational complexity. The suitability of this approach for controlling a flapping wing over a broad range of parameters is discussed.

Nomenclature

a_i^m, b_{ij}, c_{ijk}, d_i^l, d_i^h, d_i^p, $\hat{d}_i^p$, e_i^m, f_{ij}^m, g_i^{mn}, h_i^j, $\hat{h}_i^m$	=	reduced-order simulation coefficients
$\boldsymbol{C}$	=	correlation matrix
c	=	chord length
F_X, F_Y	=	force coefficients
f	=	flapping frequency
h	=	nondimensional heave amplitude, $\equiv \bar{Y}_{\max}/c$
k	=	reduced frequency, $= 2\pi fc/U_\infty$
l	=	nondimensional lag amplitude, $\equiv \bar{X}_{\max}/c$
$\boldsymbol{Q}$, $\boldsymbol{q}_j$	=	eigenvectors of proper orthogonal decomposition (POD)
t	=	nondimensional time
$\boldsymbol{U}$, $\boldsymbol{u}^k$	=	velocity snapshot
U_∞	=	freestream velocity
$\hat{\boldsymbol{u}}$	=	projection of velocity snapshot
$\tilde{\boldsymbol{u}}$	=	simulated (reduced-order) velocity field
V_0	=	heave velocity, $\equiv kh\cos kt$
X, Y	=	coordinates in inertial frame
X_0, Y_0	=	nondimensional coordinates of airfoil in inertial frame
x, y	=	coordinates in noninertial frame
y_j	=	POD mode coefficient
γ_h	=	heave control mode coefficient
γ_l	=	lag control mode coefficient
γ_p	=	pitch control mode coefficient
δ, ϵ	=	pitch and lag phase parameters
ϵ_p	=	projection error
ϵ_s	=	simulation error
ϵ_t	=	total error
θ	=	airfoil pitch angle
Λ, λ_j	=	eigenvalues of POD decomposition
$\boldsymbol{\Phi}_j$	=	jth POD mode

Received 11 February 2004; revision received 12 August 2004; accepted for publication 13 August 2004.

*Research Assistant, Department of Mechanical and Aerospace Engineering; currently Research Engineer, Avir Sensors, 310 4th Street NE, Suite 201, Charlottesville, VA 22902; gregory.lewin@alumni.carleton.edu. Member AIAA.

†Professor, Department of Mechanical and Aerospace Engineering, P.O. Box 400746; haj-hariri@virginia.edu.

Introduction

THE increased computational power of modern microprocessors has made the concept of active control of time-dependent flows technically feasible. In contrast with passive control, where control surfaces interact with steady or quasi-steady flow features, active control involves the interaction of control actuation with the unsteady components inherent in the flow at similar timescales. One potential application of active control is the control of flapping wings, particularly for microaerial vehicles (MAVs). As the wing span of a MAV shrinks, the lift generated by fixed wings is not sufficient to maintain flight. Many have envisioned very small, flapping winged robots as the next generation of MAVs.[1]

Recent experimental studies have shown that the aerodynamic forces generated by flapping insects are very sensitive to the wing kinematics. For instance, relatively subtle changes in the wing motion of a butterfly, Vanessa atalanta, from flap to flap can radically change the forces on the wing.[2] Further, small changes in wing kinematics of the fruit fly *Drosophila melanogaster* are sufficient to produce the large forces necessary for rapid turning motions.[3] Given these observations, it is clear that the propulsion and maneuvering of MAVs will require an active control system that can operate at timescales on the order of a flap or less.

The active control of fluids is by its nature highly complex. For a flapping wing, there are an infinite number of spatial modes of infinite extent, but actuation of these modes is limited to localized motions of the airfoil. If the problem is viewed in terms of the important outputs (i.e., thrust, lift, pitching moment, etc.), then it can be cast as a traditional controls problem (e.g., maximize efficiency subject to some power and force constraints), although the relationship between inputs and outputs is extremely complicated. Several traditional computational-fluid-dynamic (CFD) models have been developed to analyze the dynamics of small-scale flapping flight[4–6]; however, because they are computationally intensive Navier–Stokes (N-S) solvers are not suited for active control of fluids. Alternatively, reduced-order models can be used to simplify the problem and drastically reduce the required computational resources. Reduced-order models, however, result in the loss of some information about the flow, thus adding another level of approximation to the problem.

The focus of this paper is the development of a reduced-order model that can potentially be used in the active control of a flapping wing. One method of reduced-order modeling that has shown promise uses proper orthogonal decomposition (POD; described in the next section) to generate a set of orthogonal modes from a series

of "snapshots" from one or more flows. These modes can then be used in a Galerkin projection of the governing equations, and control modes can be used to drive the system at various flapping parameters. The POD basis functions are optimal in the sense that any given set of modes contains more energy than any other orthogonal decomposition. Using POD, it is possible to represent a complex flow using only a few basis functions, as opposed to the thousands of mesh points needed to determine a flow using traditional CFD.

Several authors have attempted to demonstrate the usefulness of POD for simulating and controlling canonical fluid problems, including the driven cavity problem,[7–10] the wake behind a circular cylinder,[11–14] flow in a grooved channel,[11] and Rayleigh–Bénard convection.[15]

Depending on the problem, the number and variety of snapshots used to generate the POD modes can have a strong influence on the robustness of the model. For flow around a circular cylinder, the wavelengths of the wake structures are strongly affected by the Reynolds number. Thus, POD modes generated from a CFD simulation are only useful within a narrow parameter range near that CFD simulation.[11] On the other hand, for flow in a grooved channel the horizontal wave number is primarily determined by the channel periodicity, and thus active control simulations can produce reasonable results over a wide variety of Reynolds numbers. Similarly, Arian et al.[9] noted that for the driven cavity problem, when the control input is far from the CFD simulation used to parameterize the model, large errors are introduced into the approximated solution. This can be circumvented by resolving the full N-S equations to generate a new mode set when the control input varies significantly. Graham et al.[12,13] found a similar problem while studying the control of the wake behind a circular cylinder using rotational motions. When the POD modes were generated from snapshots at a given oscillation frequency, the active control model breaks down unless the control input is very near this frequency. However, by using a frequency "chirp" to generate the flow snapshots more information is contained in the POD modes, and a wider range of control inputs can be simulated.

The present work demonstrates the application of POD to generate a reduced-order model of a heaving airfoil. After formulating the problem, we present the derivation of the reduced-order model. This is followed by the examination of a number of test cases and a description of efforts to enhance the parameter range of the model.

Problem Definition

Consider a rigid, two-dimensional airfoil undergoing prescribed, periodic, flapping motions in an incompressible, viscous flow with constant horizontal freestream velocity U_∞. The flapping consists of heaving (vertical), lagging (horizontal), and pitching (angular) motions. Assume the airfoil is in cruise condition: level flight with constant average velocity U_∞, that is, the airfoil is not allowed any net acceleration, but is analogous to a mechanical wing in a wind tunnel.

For computational simplicity, the problem is formulated in a noninertial reference frame fixed to the airfoil such that the origin coincides with the pitch axis, the x axis is fixed parallel to the chord, and the y axis is perpendicular to both the x axis and the span (Fig. 1). In the inertial frame, the X axis is horizontal (mean flow direction), and the Y axis is vertical. The nondimensional horizontal, vertical, and angular positions of the airfoil are denoted by X_0, Y_0, and θ, respectively, where the first two are made nondimensional by dividing the absolute position by the chord length c.

Introducing the reduced frequency $k = 2\pi f c/U_\infty$, the position of the airfoil for sinusoidal motions is given by

$$Y_0 = h\sin kt, \qquad X_0 = l\sin(kt-\delta)$$

$$\theta = \theta_{\max}\sin(kt-\epsilon) \tag{1}$$

By differentiating Eq. (1), the dimensionless heave velocity can be expressed as $V_0 \equiv \partial Y_0/\partial t$.

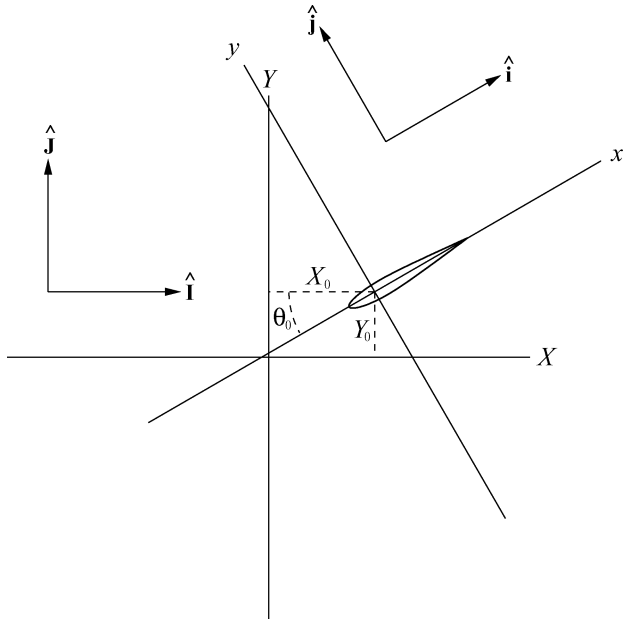

Fig. 1 Newtonian and airfoil-based coordinate systems.

Derivation of the Reduced-Order Model

Proper Orthogonal Decomposition

Proper orthogonal decomposition, also known as Karhunen–Loeve expansion, has been widely used to identify coherent structures in turbulent flows and examine their stability (see Holmes et al. [16] for a review). With POD, a set of spatial modes is produced from a series of flow snapshots generated by either computational or experimental means. Either the vorticity field ζ or the velocity field $\boldsymbol{u}$ can be used for the POD. When velocity is used, the eigenvalues of the decomposition are a direct measure of the kinetic energy contained in each mode, and the POD basis functions are optimal in the sense that they capture the most kinetic energy possible for a given number of orthogonal modes. The velocity formulation proved superior to the vorticity formulation for the current work, and only the derivation of the former is provided here.

Let $\boldsymbol{u}^k(\boldsymbol{x})$, $(1 \le k \le N)$ represent a set of snapshots of the velocity field over domain D, each at time $k\Delta t$, and let

$$\langle \boldsymbol{u}^i, \boldsymbol{u}^j \rangle \equiv \int_D \boldsymbol{u}^i \cdot \boldsymbol{u}^j \, \mathrm{d}\boldsymbol{x}$$

be the inner product. A correlation matrix $\boldsymbol{C}$ can be constructed from the snapshots using

$$\boldsymbol{C}_{ij} = \langle \boldsymbol{u}^i, \boldsymbol{u}^j \rangle$$

The POD modes are found by first solving the eigenvalue problem

$$\boldsymbol{CQ} = \boldsymbol{Q}\Lambda$$

for the matrix of eigenvectors $\boldsymbol{Q}$ and the eigenvalues Λ. By construction $\boldsymbol{C}$ is nonnegative Hermitian, and thus $\boldsymbol{Q}$ is orthogonal. For each eigenvalue of $\boldsymbol{C}$, λ_j, there is a corresponding mode $\boldsymbol{\Phi}_j$, defined by

$$\boldsymbol{\Phi}_j = 1\Big/\sqrt{\lambda_j}\,\boldsymbol{U}\boldsymbol{q}_j$$

where $\boldsymbol{U}$ is the matrix of N snapshots $\{\boldsymbol{u}^1, \boldsymbol{u}^2, \ldots, \boldsymbol{u}^N\}$ and $\boldsymbol{q}_j$ is the jth eigenvector, normalized such that $\langle \boldsymbol{\Phi}_i, \boldsymbol{\Phi}_j \rangle = \delta_{ij}$ (δ_{ij} being the Krónecker delta). Using J modes (where $J \le N$), ordered by decreasing λ_j, the snapshots can be approximated by

$$\boldsymbol{u}^k(\boldsymbol{x}) \approx \hat{\boldsymbol{u}}^k(\boldsymbol{x}) = \sum_{j=1}^{J} y_j(k\Delta t)\boldsymbol{\Phi}_j \tag{2}$$

where $\hat{\boldsymbol{u}}$ is the approximate velocity profile and the normalized coefficients y_j are given by

$$y_j(k\Delta t) = \left\langle \boldsymbol{u}^k, \boldsymbol{\Phi}_j \right\rangle \tag{3}$$

Equation (3) will be referred to as a projection of a solution because it is the result of projecting a snapshot $\boldsymbol{u}^k$ onto the POD modes $\boldsymbol{\Phi}_j$.

Galerkin Projection

The POD modes can be used to simulate a fluid flow by reformulating the Navier–Stokes equations using a Galerkin projection. For computational simplicity (to avoid moving boundaries), the projection is performed in the noninertial reference frame of the airfoil. Given the appropriately modified momentum transport equations,

$$\frac{\partial \boldsymbol{u}}{\partial t} = -\nabla p - (\boldsymbol{u}\cdot\nabla)\boldsymbol{u} + \frac{1}{Re}\nabla^2\boldsymbol{u} - \boldsymbol{a}_0(t) - \ddot{\theta}\hat{\boldsymbol{k}}\times\boldsymbol{r} + \dot{\theta}^2\boldsymbol{r} - 2\dot{\theta}\hat{\boldsymbol{k}}\times\boldsymbol{u} \tag{4}$$

the time-dependent velocity field $\boldsymbol{u}(\boldsymbol{x}, t)$ is expanded as

$$\boldsymbol{u}(\boldsymbol{x}, t) = \sum_{m=1}^{M}\gamma_m(t)\boldsymbol{u}_m(\boldsymbol{x}) + \sum_{j=1}^{J} y_j(t)\boldsymbol{\Phi}_j(\boldsymbol{x}) \tag{5}$$

where J is the number of POD modes and M is the number of control functions needed to simulate the desired motion (e.g., heaving, pitching, or lagging). For the solution to be written as a superposition of modes, the modes need to have homogeneous boundary conditions. Because the actual boundary conditions in either the inertial or the noninertial frame are nonhomogeneous, the control functions are simply those particular solutions that are kinematically compatible with the boundary conditions. As such, there is a multitude of options for generating control modes, and their selection is discussed next. Note that $\gamma_m(t)$ are prescribed control inputs, while $y_j(t)$ are the dependent variables of the simulation. When control functions are used, the snapshots must be modified by subtracting the control functions before the decomposition is performed:

$$\boldsymbol{u}^k_{\text{modified}} = \boldsymbol{u}^k - \sum_{m=1}^{M}\gamma_m(k\Delta t)\boldsymbol{u}_m$$

Using [ ] to represent a boundary integral {i.e., $[\boldsymbol{\Phi}_i\nabla\boldsymbol{u}] \equiv \oint_C \boldsymbol{\Phi}_i\cdot(\partial\boldsymbol{u}/\partial n)\,\mathrm{d}s$} and noting that $\langle\boldsymbol{\Phi}_i, \nabla^2\boldsymbol{u}\rangle = -\langle\nabla\boldsymbol{\Phi}_i, \nabla\boldsymbol{u}\rangle + [\boldsymbol{\Phi}_i\nabla\boldsymbol{u}]$ (where the shorthand notation $\langle\nabla\boldsymbol{\Phi}, \nabla\boldsymbol{u}\rangle$ is the equivalent of $\langle\nabla\phi_x, \nabla u\rangle + \langle\nabla\phi_y, \nabla v\rangle$), Equation (5) is projected onto the orthogonal modes $\boldsymbol{\Phi}_i$ to get

$$\left\langle\boldsymbol{\Phi}_i, \frac{\partial\boldsymbol{u}}{\partial t}\right\rangle = \langle\boldsymbol{\Phi}_i, -(\boldsymbol{u}\cdot\nabla)\boldsymbol{u}\rangle - \frac{1}{Re}\langle\nabla\boldsymbol{\Phi}_i, \nabla\boldsymbol{u}\rangle + \frac{1}{Re}[\boldsymbol{\Phi}_i\nabla\boldsymbol{u}] - \langle\boldsymbol{\Phi}_i, \boldsymbol{a}_0\rangle - \ddot{\theta}\langle\boldsymbol{\Phi}_i, \hat{\boldsymbol{k}}\times\boldsymbol{r}\rangle + \dot{\theta}^2\langle\boldsymbol{\Phi}_i, \boldsymbol{r}\rangle - 2\dot{\theta}\langle\boldsymbol{\Phi}_i, \hat{\boldsymbol{k}}\times\boldsymbol{u}\rangle \tag{6}$$

The pressure term does not add any terms to Eq. (6). Because the modes are linear combinations of the divergence-free snapshots, each mode is itself divergence free. Therefore, one can write

$$\langle\boldsymbol{\Phi}_i, \nabla p\rangle = \langle\nabla\cdot(p\boldsymbol{\Phi}_i), 1\rangle = [p\boldsymbol{\Phi}_i] \approx 0$$

The last step follows from the fact that the velocity on the airfoil is zero in the noninertial reference frame, and the pressure at the outer boundary is considered negligible.

By orthogonality, the left-hand side of Eq. (6) reduces to

$$\left\langle\boldsymbol{\Phi}_i, \frac{\partial\boldsymbol{u}}{\partial t}\right\rangle = \sum_{m=1}^{M}\frac{\partial\gamma_m}{\partial t}\langle\boldsymbol{\Phi}_i, \boldsymbol{u}_m\rangle + \frac{\partial y_i}{\partial t}$$

The first term on the right-hand side of Eq. (6) becomes

$$\langle\boldsymbol{\Phi}_i, -(\boldsymbol{u}\cdot\nabla)\boldsymbol{u}\rangle = -\sum_{m=1}^{M}\gamma_m \times\left[\sum_{n=1}^{M}\gamma_n\langle\boldsymbol{\Phi}_i, (\boldsymbol{u}_m\cdot\nabla)\boldsymbol{u}_n\rangle + \sum_{j=1}^{J} y_i\langle\boldsymbol{\Phi}_i, (\boldsymbol{u}_m\cdot\nabla)\boldsymbol{u}_j\rangle\right] - \sum_{j=1}^{J} y_j\left[\sum_{m=1}^{M}\gamma_m\langle\boldsymbol{\Phi}_i, (\boldsymbol{u}_j\cdot\nabla)\boldsymbol{u}_m\rangle + \sum_{k=1}^{J} y_k\langle\boldsymbol{\Phi}_i, (\boldsymbol{u}_j\cdot\nabla)\boldsymbol{u}_k\rangle\right]$$

The diffusive terms become

$$-\langle\nabla\boldsymbol{\Phi}_i, \nabla\boldsymbol{u}\rangle + [\boldsymbol{\Phi}_i, \nabla\boldsymbol{u}] = \sum_{m=1}^{M}\gamma_m\{-\langle\nabla\boldsymbol{\Phi}_i, \nabla\boldsymbol{u}_m\rangle + [\boldsymbol{\Phi}_i\nabla\boldsymbol{u}_m]\} + \sum_{j=1}^{J} y_j\{-\langle\nabla\boldsymbol{\Phi}_i, \nabla\boldsymbol{u}_j\rangle + [\boldsymbol{\Phi}_i\nabla\boldsymbol{u}_j]\}$$

Finally, the acceleration terms reduce to

$$\langle\boldsymbol{\Phi}_i, -\boldsymbol{a}_0\rangle = -a_x\langle\boldsymbol{\Phi}_i, \hat{\boldsymbol{i}}\rangle - a_y\langle\boldsymbol{\Phi}_i, \hat{\boldsymbol{j}}\rangle$$

$$\langle\boldsymbol{\Phi}_i, -\ddot{\theta}\hat{\boldsymbol{k}}\times\boldsymbol{r}\rangle = -\ddot{\theta}\langle\boldsymbol{\Phi}_i, \hat{\boldsymbol{k}}\times\boldsymbol{r}\rangle, \qquad \left\langle\boldsymbol{\Phi}_i, \dot{\theta}^2\boldsymbol{r}\right\rangle = \dot{\theta}^2\langle\boldsymbol{\Phi}_i, \boldsymbol{r}\rangle$$

$$\langle\boldsymbol{\Phi}_i, -2\dot{\theta}\hat{\boldsymbol{k}}\times\boldsymbol{u}\rangle = -2\dot{\theta}\left[\sum_{m=1}^{M}\gamma_m\langle\boldsymbol{\Phi}_i, \hat{\boldsymbol{k}}\times\boldsymbol{u}_m\rangle + \sum_{j=1}^{J} y_j\langle\boldsymbol{\Phi}_i, \hat{\boldsymbol{k}}\times\boldsymbol{u}_j\rangle\right]$$

For the flapping airfoil, the prescribed control inputs are heaving, lagging, and angular (pitching) velocity, so that, using the control notation of Eq. (5),

$$\gamma_h = V_y, \qquad \gamma_l = V_x, \qquad \gamma_p = \dot{\theta}$$

After some algebra, the N-S equations are reduced to the following set of ordinary differential-equations (ODEs):

$$\frac{\partial y_i}{\partial t} = \sum_{m=1}^{M}\frac{\partial\gamma_m}{\partial t}a_i^m + \frac{1}{Re}\sum_{j=1}^{J} y_j b_{ij} + \sum_{j=1}^{J}\sum_{k=1}^{J} y_j y_k c_{ijk} + \sum_{m=1}^{M}\frac{\partial\gamma_m}{\partial t}d_i^m + \gamma_p^2\hat{d}_i^p + \frac{1}{Re}\sum_{m=1}^{M}\gamma_m e_i^m + \sum_{m=1}^{M}\sum_{j=1}^{J}\gamma_m y_j f_{ij}^m + \sum_{m=1}^{M}\sum_{n=1}^{M}\gamma_m\gamma_n g_i^{mn} + \gamma_p\left[\sum_{j=1}^{J} y_j h_i^j + \sum_{m=1}^{M}\gamma_m\hat{h}_i^m\right] \tag{7}$$

where

$$a_i^m = -\langle\boldsymbol{\Phi}_i, \boldsymbol{u}_m\rangle, \qquad b_{ij} = -\langle\nabla\boldsymbol{\Phi}_i, \nabla\boldsymbol{u}_j\rangle + [\boldsymbol{\Phi}_i\nabla\boldsymbol{u}_j]$$

$$c_{ijk} = -\langle\boldsymbol{\Phi}_i, (\boldsymbol{u}_j\cdot\nabla)\boldsymbol{u}_k\rangle, \qquad d_i^l = -\langle\boldsymbol{\Phi}_i, \hat{\boldsymbol{i}}\rangle, \qquad d_i^h = -\langle\boldsymbol{\Phi}_i, \hat{\boldsymbol{j}}\rangle$$

$$d_i^p = -\langle\boldsymbol{\Phi}_i, \hat{\boldsymbol{k}}\times\boldsymbol{r}\rangle, \qquad \hat{d}_i^p = \langle\boldsymbol{\Phi}_i, \boldsymbol{r}\rangle$$

$$e_i^m = -\langle\nabla\boldsymbol{\Phi}_i, \nabla\boldsymbol{u}_m\rangle + [\boldsymbol{\Phi}_i\nabla\boldsymbol{u}_m]$$

$$f_{ij}^m = -\langle\boldsymbol{\Phi}_i, (\boldsymbol{u}_j\cdot\nabla)\boldsymbol{u}_m\rangle - \langle\boldsymbol{\Phi}_i, (\boldsymbol{u}_m\cdot\nabla)\boldsymbol{u}_j\rangle$$

$$g_i^{mn} = -\langle\boldsymbol{\Phi}_i, (\boldsymbol{u}_m\cdot\nabla)\boldsymbol{u}_n\rangle, \qquad h_i^j = -2\langle\boldsymbol{\Phi}_i, \hat{\boldsymbol{k}}\times\boldsymbol{u}_j\rangle$$

$$\hat{h}_i^m = -2\langle\boldsymbol{\Phi}_i, \hat{\boldsymbol{k}}\times\boldsymbol{u}_m\rangle \tag{8}$$

where the superscripts m and n can refer to any of the motions being controlled. Equations (7) and (8) constitute an initial value problem with coupled, nonlinear ODEs with constant coefficients a_i^m, b_{ij}, etc. Solving these equations with a suitable time-stepping algorithm will be referred to as a reduced-order simulation. The velocity field produced by solving these equations will be denoted by $\tilde{\boldsymbol{u}}(\boldsymbol{x}, t)$.

Definition of Errors

Following Graham et al.,[12] errors are classified into two categories, projection errors and simulation (prediction) errors. Projection errors result from the inability to exactly recreate a snapshot using the POD modes of a given simulation. For this work, the

projection error is defined as

$$\epsilon_p = \frac{\langle \boldsymbol{u} - \hat{\boldsymbol{u}}, \boldsymbol{u} - \hat{\boldsymbol{u}} \rangle}{\left\langle \boldsymbol{u} - \sum_{m=1}^{M} \gamma_m \boldsymbol{u}_m, \boldsymbol{u} - \sum_{m=1}^{M} \gamma_m \boldsymbol{u}_m \right\rangle} \tag{9}$$

Note that normalization is based on the fluctuations

$$\boldsymbol{u} - \sum_{m}^{M} \gamma_m \boldsymbol{u}_m$$

so that the error is not swamped by the energy contained in the control functions.

Simulation errors result from errors in y_i generated in the reduced-order simulation. They include discretization errors, numerical (round-off) errors, and most important, errors resulting from the loss of information about the flow during the POD. The simulation error is defined as the difference between the total error and the projection error $\epsilon_s = \epsilon_t - \epsilon_p$, where the total error is given by

$$\epsilon_t = \frac{\langle \boldsymbol{u} - \tilde{\boldsymbol{u}}, \boldsymbol{u} - \tilde{\boldsymbol{u}} \rangle}{\left\langle \boldsymbol{u} - \sum_{m=1}^{M} \gamma_m \boldsymbol{u}_m, \boldsymbol{u} - \sum_{m=1}^{M} \gamma_m \boldsymbol{u}_m \right\rangle} \tag{10}$$

Ultimately, the measure of the success of the model will be its ability to reproduce the forces and moment on the airfoil. Within this work, force comparisons are made using force portraits, which show the X and Y components of the total force on separate axes (see the following).

Control Modes

Although the restrictions on the control functions are fairly loose, the actual control functions chosen can have a marked effect on the accuracy of the method. The control functions are required to be divergence free and need only satisfy the appropriate boundary conditions; otherwise, they are arbitrary.

Several methods were used to generate candidate control functions. The simplest was to start an airfoil impulsively with the desired motion in a quiescent fluid and use an arbitrary snapshot from the generated flowfield. Alternative control functions were generated by oscillating the airfoil and subtracting either the mean flow or the flow around a stationary airfoil (so that the net flow for the control function contains no freestream velocity). Figure 2 shows the vorticity field for a pair of potential heaving control functions: a snapshot of an impulsively started flow and the result of subtracting the flow about a stationary airfoil from the snapshot of an oscillating airfoil. (Although the velocity field was used in the POD, the vorticity field makes for a better visualization.)

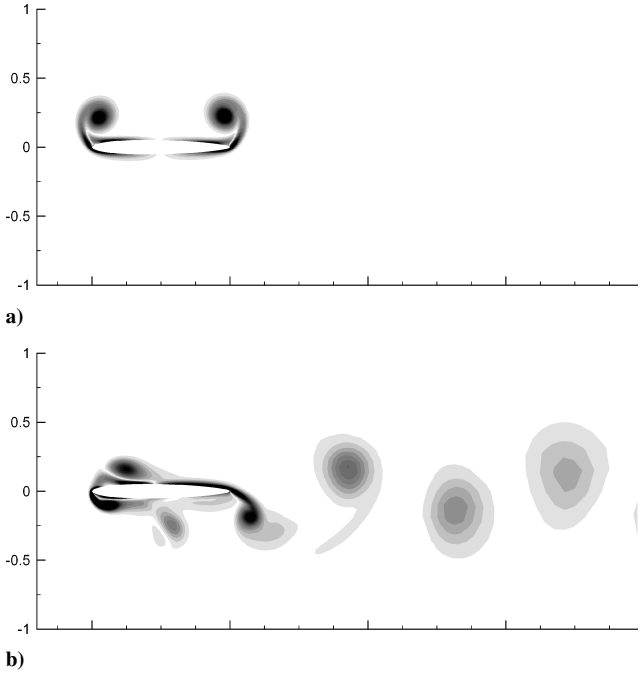

Fig. 2 Potential heaving control functions generated from a) an impulsively started airfoil and b) a snapshot from a CFD simulation with $k = 5.0$, $h = 0.2$ less the flow about a stationary airfoil.

Both of these functions and several others were tested using reduced-order simulations with $k = 5.0$, $h = 0.2$. Figure 3 shows a comparison between selected vorticity snapshots from the CFD and reduced-order simulations using the control function in Fig. 2b. Note that the vorticity fields agree well, with small variations at the finer scales. Figure 4 shows a comparison of the coefficients of the two most energetic modes for the same simulations. The modes from the reduced-order simulation track the projected solution almost exactly.

The excellent agreement among the mode coefficients from the projection and the reduced-order simulations leads to very small simulation errors, as shown in Fig. 5b. Although the errors using the control function from the impulsively started airfoil are also low (Fig. 5a), using a heaving airfoil less the stationary flow reduces the errors substantially. Of all of the heaving control functions tested, the function shown in Fig. 2b produced the lowest error.

Note that the control function was generated from a simulation with heaving parameters identical to the test case. To be sure that this did not bias the results, the same control function was used in reduced-order simulations with $k = 3.0$ and 6.25. No significant increase in errors was found in either case. Thus, the function in Fig. 2b was chosen as the heaving control function for all simulations.

Results of the POD/Reduced-Order Simulations

The reduced-order model just described was used to simulate a heaving airfoil at a variety of frequencies and amplitudes. For each of the cases presented, the POD modes were created by decomposing snapshots created from a CFD model described by the current authors.[6] The CFD simulations were performed on an O-type grid with 256 grid points in the radial direction and 128 grid points in the circumferential direction. For the POD and reduced-order simulations 128 grid points in the circumferential direction were used, but only the 128 grid points nearest the airfoil in the radial direction were retained. This subset was used to reduce the computational resources for pre- and postprocessing. Because little variation in energy is found in the domain far from the airfoil, the contribution of this region to the overall results is minimal. The CFD simulations were run until the flowfield within the POD subdomain became periodic, that is, the initial starting vortices were well beyond the boundary of the POD domain. The reduced-order simulations used a second-order Runge–Kutta method time integration with the same time step as the CFD simulations.

Within each section that follows, a number of reduced-order simulations are performed for several sets of heaving parameters. Differences in the simulations reflect the variety of snapshots used to generate the POD modes. The starting condition for each reduced-order simulation is the projection of the CFD solution at the beginning of the last flap. Thus, the reduced-order simulation and the corresponding CFD simulation used for comparison overlap for one flap. The accuracy of a reduced-order simulation is assessed by noting the simulation and projection errors and by comparing the forces from the CFD simulation to the reduced-order simulation.

This demonstration of the reduced-order approach focuses on heaving only. For certain heaving parameters the flow can be asymmetric or aperiodic.[6] The aperiodic solutions cause serious problems for the POD approach because the number of flaps (and thereby snapshots) required to include all of the information in the flow grows substantially (infinitely, for chaotic solutions). Additionally, the asymmetric flows are dependent on starting conditions. Therefore, only the symmetric, periodic simulations will be discussed here; chaotic flows can be stabilized by including a pitching component and will be investigated in a future contribution.

Number of Snapshots and Modes

Among other factors, the accuracy of a reduced-order simulation is dependent on both the number of modes retained in the simulation and the number of snapshots used to generate these modes.

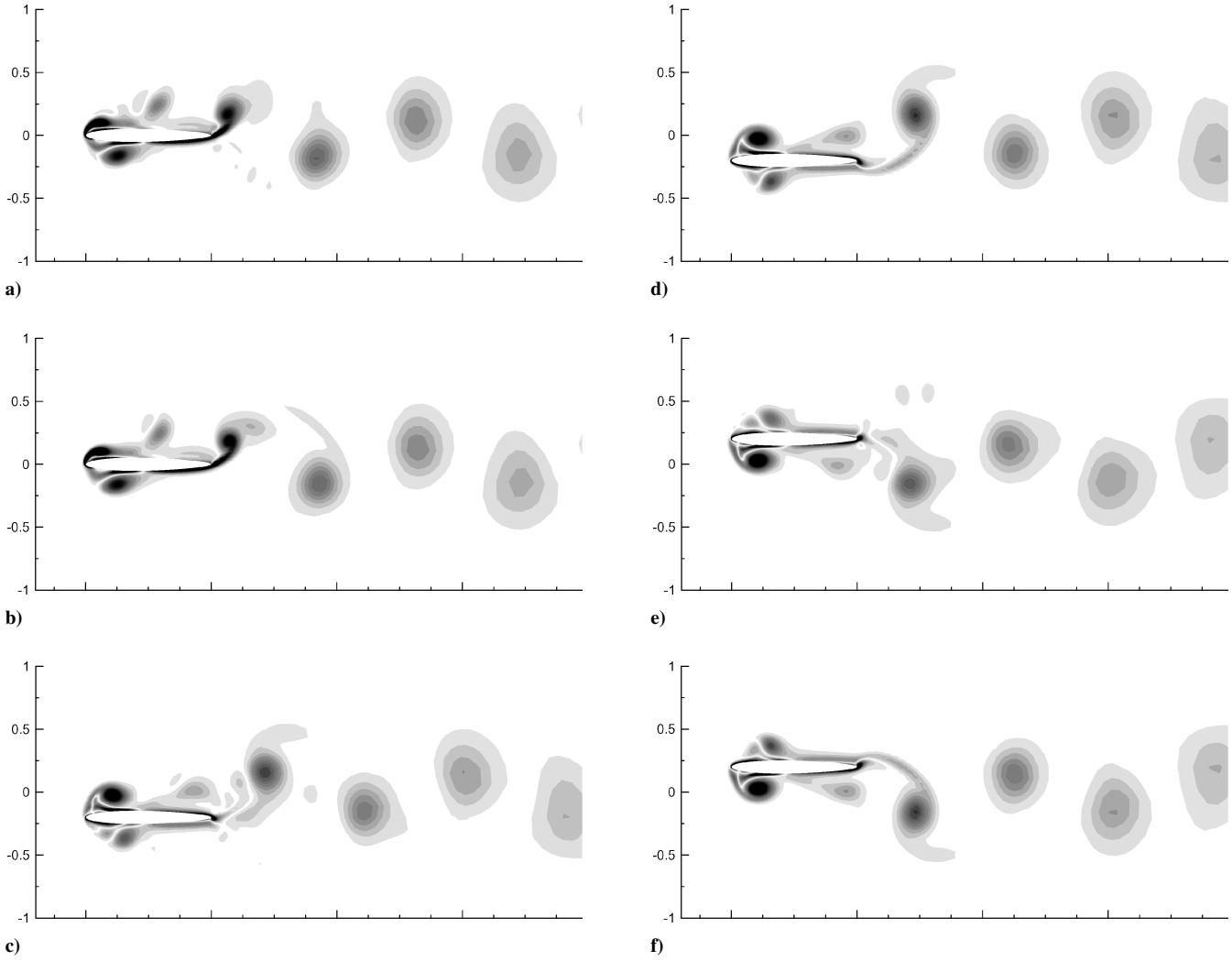

Fig. 3 Comparison of the vorticity field of a CFD simulation with a reduced-order simulation with $k = 5.0$, $h = 0.2$: a) reduced-order simulation and b) CFD simulation after $\frac{1}{4}$ flap; c) reduced-order simulation and d) CFD simulation after $\frac{1}{2}$ flap; and e) reduced-order simulation and f) CFD simulation after one full flap.

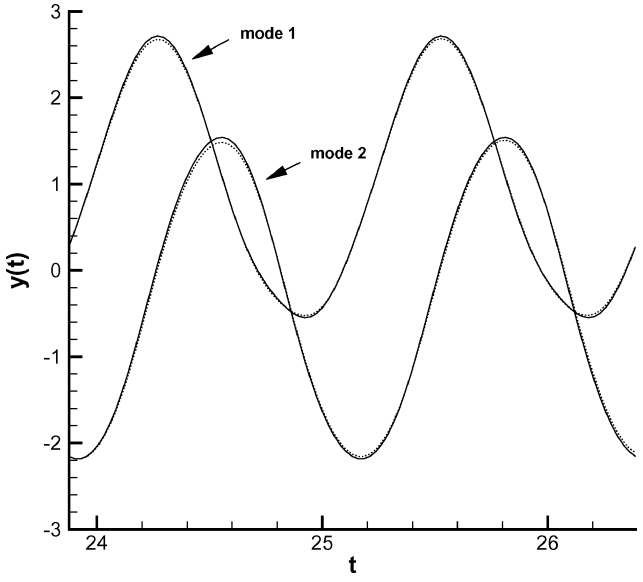

Fig. 4 Comparison of projected and simulated mode coefficients for the two most energetic modes of a simulation at $k = 5.0$, $h = 0.2$.

Increasing the number of modes increases the dimension of the solution space that can be spanned and reduces the projection error. Using more snapshots to generate the POD modes increases the information included in the modes; as the number of snapshots is increased, the dynamics of finer flow details can be captured. Of course, computational power and availability of computer memory effectively limit the number of modes and snapshots that can be used. As an example, a reduced-order simulation with 10 modes typically takes ≈2.1 s per flap using a 400-MHz Intel Pentium machine running Linux while a 20-mode simulation takes ≈10.8 s per flap. (In comparison, the full CFD simulation takes ≈3.5 h per flap on the same machine.)

To investigate their effect on accuracy, the number of snapshots and number of modes were varied over several test simulations at $k = 5.0$ and $h = 0.2$. Figure 6 shows the projection, simulation, and total errors for simulations with different numbers of modes (using 48 snapshots to create the modes). The number of modes retained in each simulation is based on the ratio of the eigenvalue of the lowest retained mode λ_J to the highest eigenvalue λ_1: for the simulation with three modes, each mode has at least 10^{-1} the energy of the highest mode; $\lambda_J/\lambda_1 \approx 10^{-2}$ for seven modes, $\lambda_J/\lambda_1 \approx 10^{-3}$ for 11 modes, and $\lambda_J/\lambda_1 \approx 10^{-4}$ for 15 modes.

As expected, as the number of modes is increased, the projection error is reduced. Using three modes, the bulk of the error is

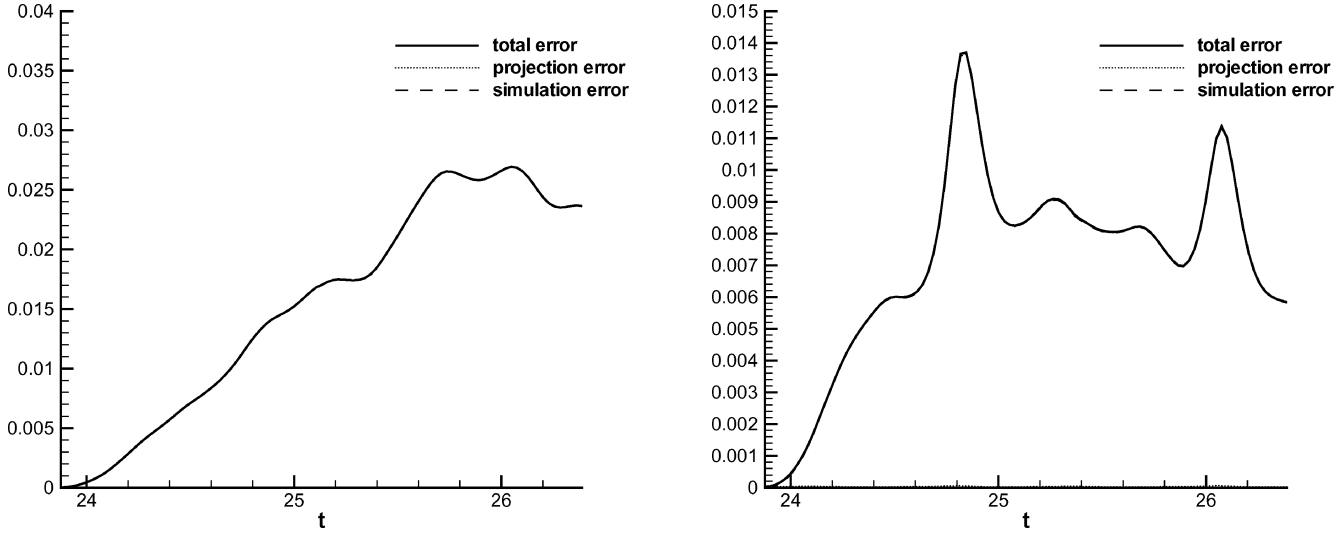

Fig. 5 Comparison between projected and simulated mode coefficients for simulation with $k = 5.0$ and $h = 0.2$ using the control functions from Fig. 2: a) impulsively started airfoil; b) snapshot less stationary flow. (Note that the projection error for this case is essentially zero and the simulation error is overlaid by the total error.)

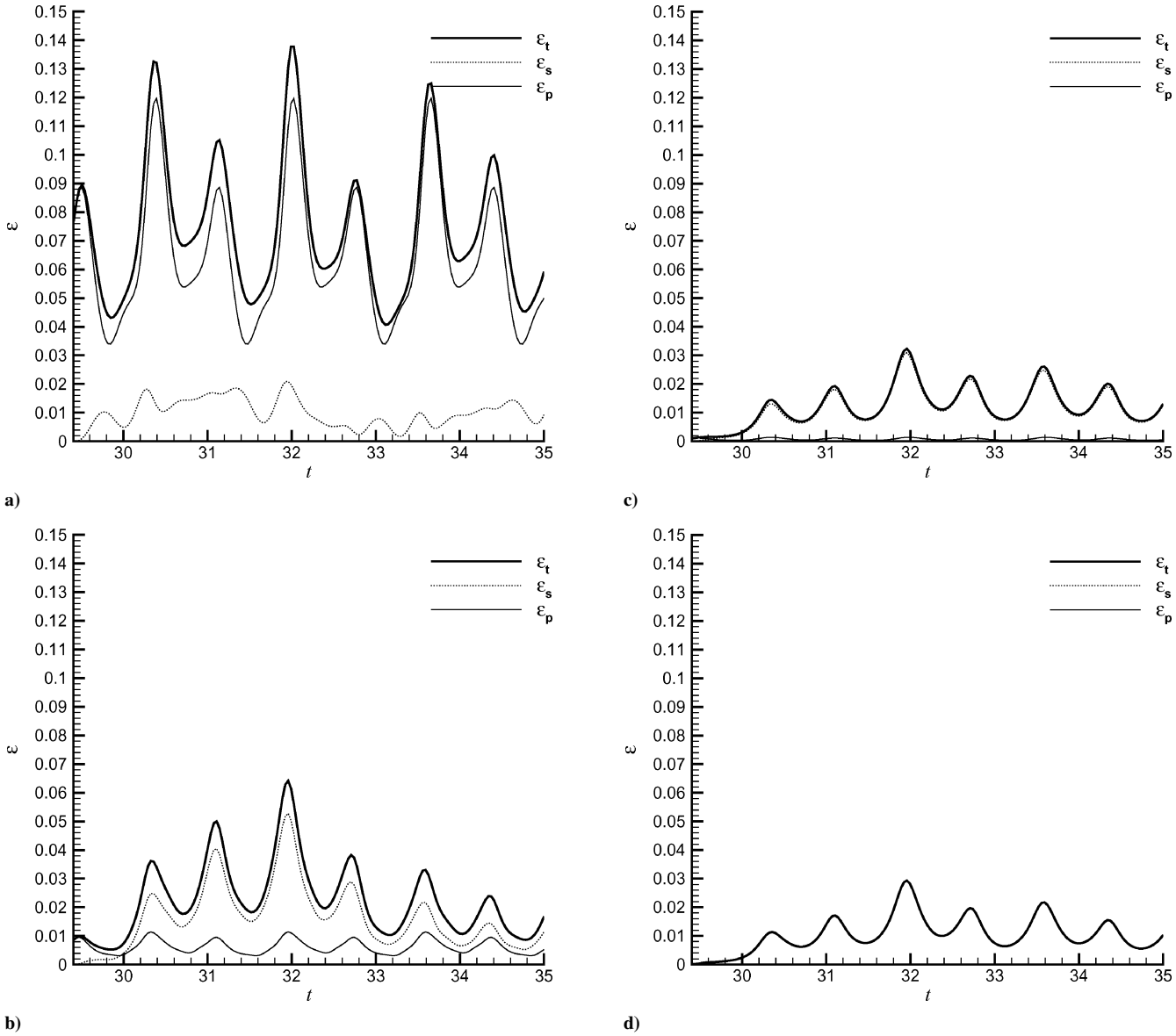

Fig. 6 Projection, simulation, and total errors vs number of modes for a reduced-order simulation with $k = 3.85$ and $h = 0.2$: a) three, b) seven, c) 11, and d) 15 modes.

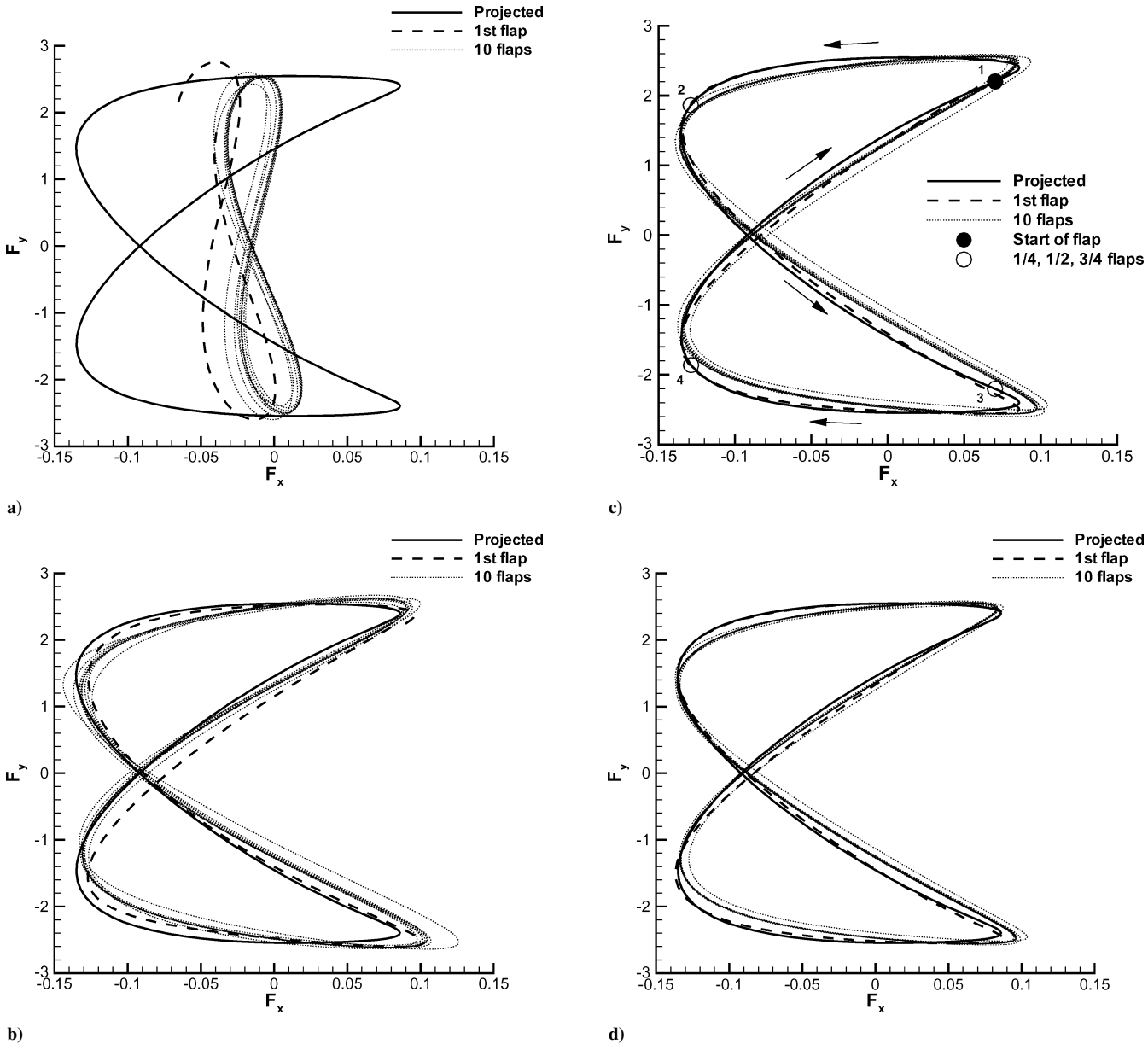

Fig. 7 Forces in the X and Y directions vs number of modes for a reduced-order simulation with $k = 3.85$ and $h = 0.2$: a) three, b) seven, c) 11, and d) 15 modes.

projection error, whereas for 15 modes the projection error is nearly zero. However, increasing the number of modes does not necessarily decrease the total error for the duration of the simulation; as will be seen in subsequent sections, simulations that retain many POD modes can have much higher long-term errors than simulations with fewer POD modes.

As shown in Fig. 7, the agreement of the forces on the airfoil mimics the errors shown in Fig. 6, in that large errors in the coefficients y_i lead to large deviations in forces. These "force portraits" will be used frequently in this work and show the forces in both the X and Y directions for several flaps. The heavy, solid line shows the forces from the CFD simulation with the same flapping parameters as the reduced-order simulation. The heavy, dashed line shows the forces for the first flap of the reduced-order simulation, and the lighter, dotted line shows all subsequent flaps. (Each simulation typically lasts 10 flaps.) In Fig. 7c, arrows have been placed to show the general orbit of the forces. Point 1 on this figure represents the beginning of a stroke when the airfoil is at its maximum positive excursion from the mean line. Points 2, 3, and 4 denote when the airfoil is at the mean line of the downstroke, the maximum negative excursion, and the mean line of the upstroke, respectively. The dots and arrows are omitted from the remaining figures because the orbits are all similar.

To investigate the effect of the number of snapshots used to generate the POD modes, several simulations were performed using different numbers of snapshots in the decomposition (not shown). As expected, the simulation error typically increases when fewer snapshots are included in the decomposition; using 11 POD modes, the maximum total error over five strokes was 0.045 for 12 snapshots compared to 0.032 for 48. Using 48 snapshots produced results nearly identical to those using 24 snapshots. Throughout this study, 48 snapshots are used to generate the POD modes.

Variation of the Heaving Parameters

For heaving motions, three nondimensional parameters can be used to describe the flow: k, h, and Re. The Reynolds number is not expected to affect the flow significantly. Although viscous effects are dominant near the airfoil, Jones et al.[17] note that the evolution of the wake is primarily an inviscid phenomenon. The scope of this work will be limited to variations in k and h, the primary dynamic parameters of the heaving motion.

Although the physical (heaving) parameters can change continuously, the POD modes are created from snapshots of CFD simulations at discrete parameter intervals. To be a useful control model, it is necessary that a reduced-order simulation be able to

reproduce accurately the forces on the airfoil for a range of flapping parameters that may differ from those used to create the POD modes.

There are a multitude of ways to construct the POD mode sets. One can simply use POD modes generated from a single CFD simulation and then alter $\gamma(t)$ in Eq. (7) to simulate a new set of parameters. Errors will be introduced into the reduced-order simulation because the modes do not contain all of the necessary information about the new flow, that is, they do not span the solution space for the new parameters. For example, if the heaving frequency is greater in a reduced-order simulation than in the CFD simulation used to create the POD modes the wavelength of vortices in the wake will shorten and POD modes will not be able to fully reproduce the new flow. By combining snapshots from two or more CFD simulations, however, the information contained in the mode set can be enhanced. Initially, results of independent POD mode sets are presented, followed by a variety of mode sets created by using different combinations of flow snapshots.

Independent POD Sets

The simplest demonstration of control is to perform a reduced-order simulation at one set of parameters using the POD modes generated from a CFD simulation at a different set of parameters. For example, Fig. 8 shows the errors for a reduced-order simulation at $k = 3.85$, $h = 0.2$ using POD modes generated from "nearby" CFD simulations that vary in either k or h. In each case the projection error is significant, a result of the modes not being able to span the solution space of the CFD simulations. Additionally, the simulation and total errors are large, particularly when k is varied. As shown in Fig. 9, the forces track poorly, as well.

In each of these cases, k and h are varied by roughly the same percentage, indicating that the reduced-order simulation is more sensitive to changes in frequency than in amplitude. This might be expected because changes in frequency directly affect the wavelength of the wake vortices, whereas changing the amplitude has only indirect effects through changes in the mean velocity of the wake.

Combined POD Sets

The flow information in a mode set, and therefore its ability to simulate a range of parameters, can be enhanced by combining snapshots from two or more CFD simulations to generate a combined mode set. By varying the frequency of rotational oscillation of a circular cylinder, Graham et al.[12,13] were able to generate a more robust

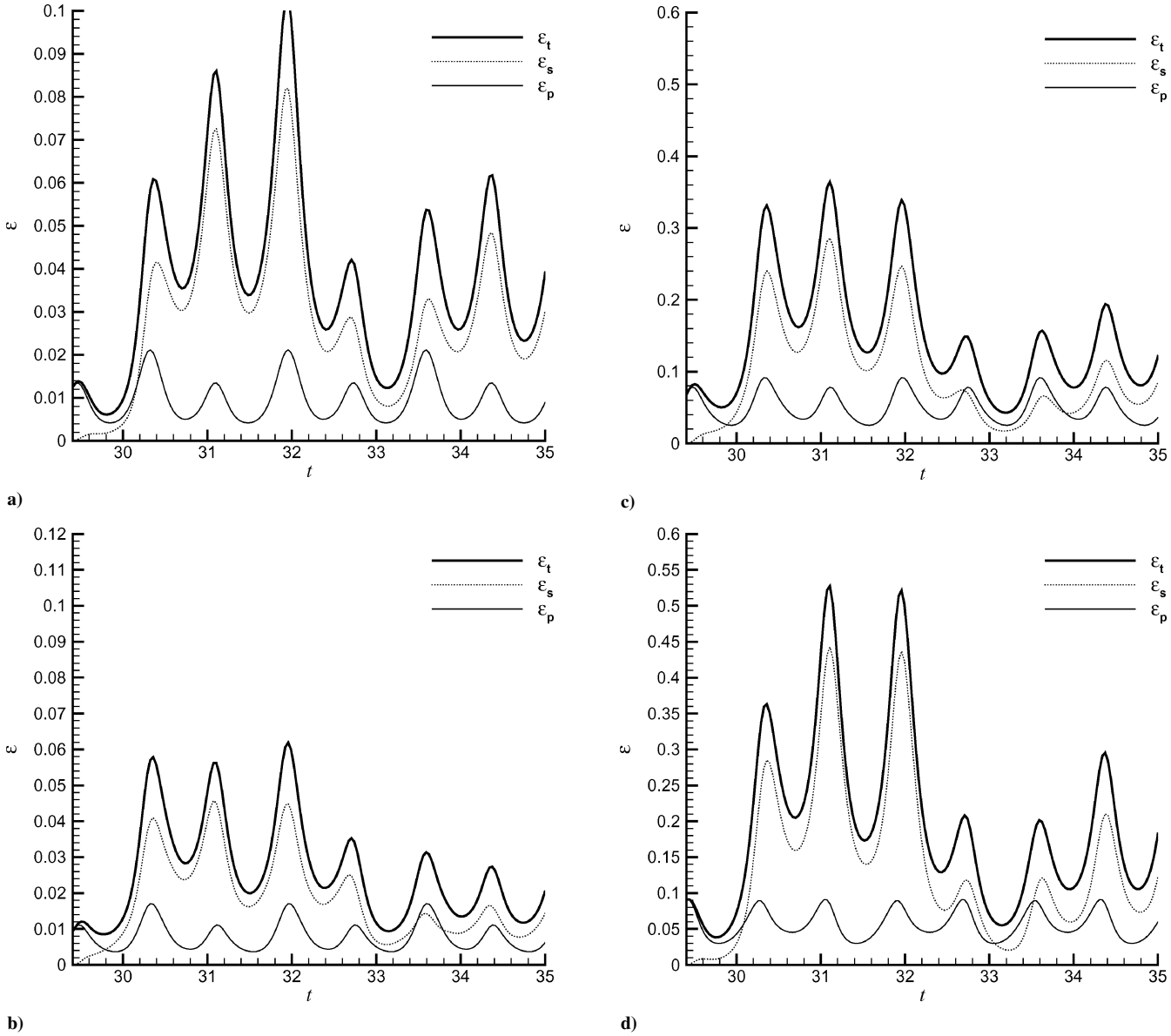

Fig. 8 Projection, simulation, and total errors for reduced-order simulations with $k = 3.85$, $h = 0.2$ using individual mode sets generated from a variety of CFD simulations: a) $k = 3.85$, $h = 0.1875$; b) $k = 3.85$, $h = 0.2125$; c) $k = 3.57$, $h = 0.2$; and d) $k = 4.17$, $h = 0.2$.

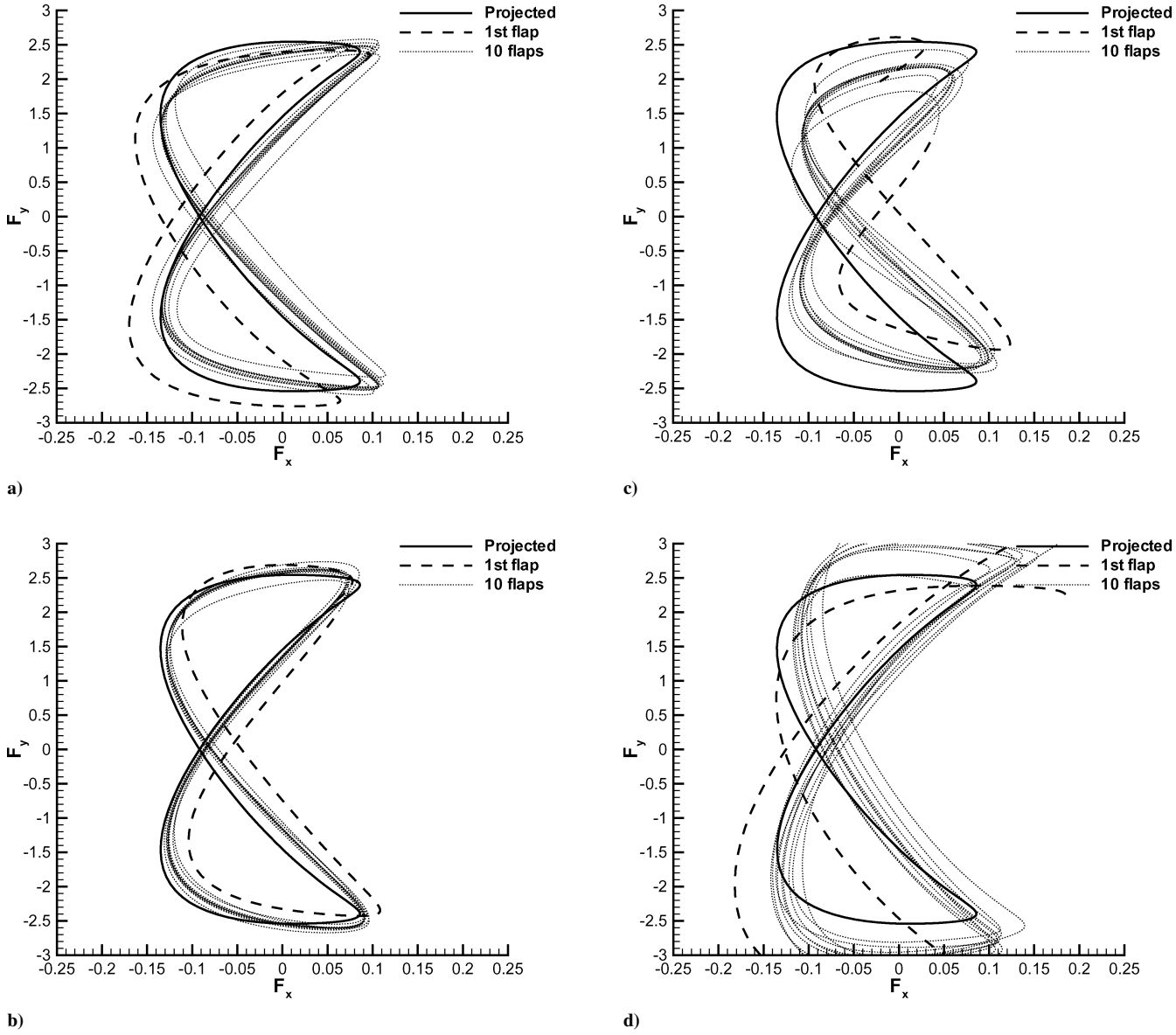

Fig. 9 Force portraits for reduced-order simulations with $k = 3.85$, $h = 0.2$ using individual mode sets generated from a variety of CFD simulations: a) $k = 3.85$, $h = 0.1875$; b) $k = 3.85$, $h = 0.2125$; c) $k = 3.57$, $h = 0.2$; and d) $k = 4.17$, $h = 0.2$.

set of POD snapshots, in that a wider range of control input could be modeled effectively. In this section, snapshots are taken from pairs of CFD simulations that "straddle" the reduced-order simulation to generate combined POD modes. For comparison, the difference in the frequency and amplitude for the CFD simulations used to create the snapshots will be denoted by Δk and Δh, respectively.

Variations in Frequency

Reduced-order simulations were performed at $k = 3.85$, $h = 0.2$ using snapshots combined from CFD simulations at frequencies slightly higher and lower than the test case. Figure 10 shows the errors and a force portrait for a reduced-order simulation with $k = 3.85$, $h = 0.2$ using modes generated from CFD results at $k = 3.57$, $h = 0.2$ and $k = 4.17$, $h = 0.2$ ($\Delta k = 0.6$). The numbers of modes used in each simulation were based on the ratio of the lowest eigenvalue retained to the highest eigenvalue (λ_J/λ_1): 10^{-2} (nine modes; Fig. 10a), 10^{-3} (18 modes; Fig. 10b), and 10^{-4} (26 modes; Fig. 10c). Note that it is necessary to retain significantly more modes for a given eigenvalue ratio than with the independent modes sets, an indication that the diversity of the snapshots is increased, diminishing the relative dominance of the most energetic modes.

Because the snapshots from the CFD simulation at the parameters of the reduced-order simulation are omitted, there is a small projection error, even when 26 modes are retained. Overall, however, the errors in the simulations are markedly less than those of the individual mode sets, as seen in Figs. 8c and 8d. Figure 10d shows the force portrait for the reduced-order simulation with 26 modes. Despite the low errors, the forces do not track well for even the first flap, with deviations in the force in the X direction approaching 30–40%.

To improve the accuracy, additional simulations were performed with frequencies nearer to the test frequency of $k = 3.85$. Figure 11 shows the errors and a force portrait for reduced-order simulations with $k = 3.85$, $h = 0.2$ using 24 modes generated from CFD results at $k = 3.70$, $h = 0.2$ and $k = 4.0$, $h = 0.2$ ($\Delta k = 0.3$). Because the snapshots are taken from CFD simulations nearer to the simulated parameters, the projection error is decreased, and a fewer number of modes are needed to meet the eigenvalue ratio criterion. The force estimates are noticeably improved, particularly for the first stroke.

The combined POD mode set was able to simulate, with comparable accuracy, heaving at several other frequencies in the range $3.7 \leq k \leq 4.0$ (results not shown). Thus, combined pairs of snapshots

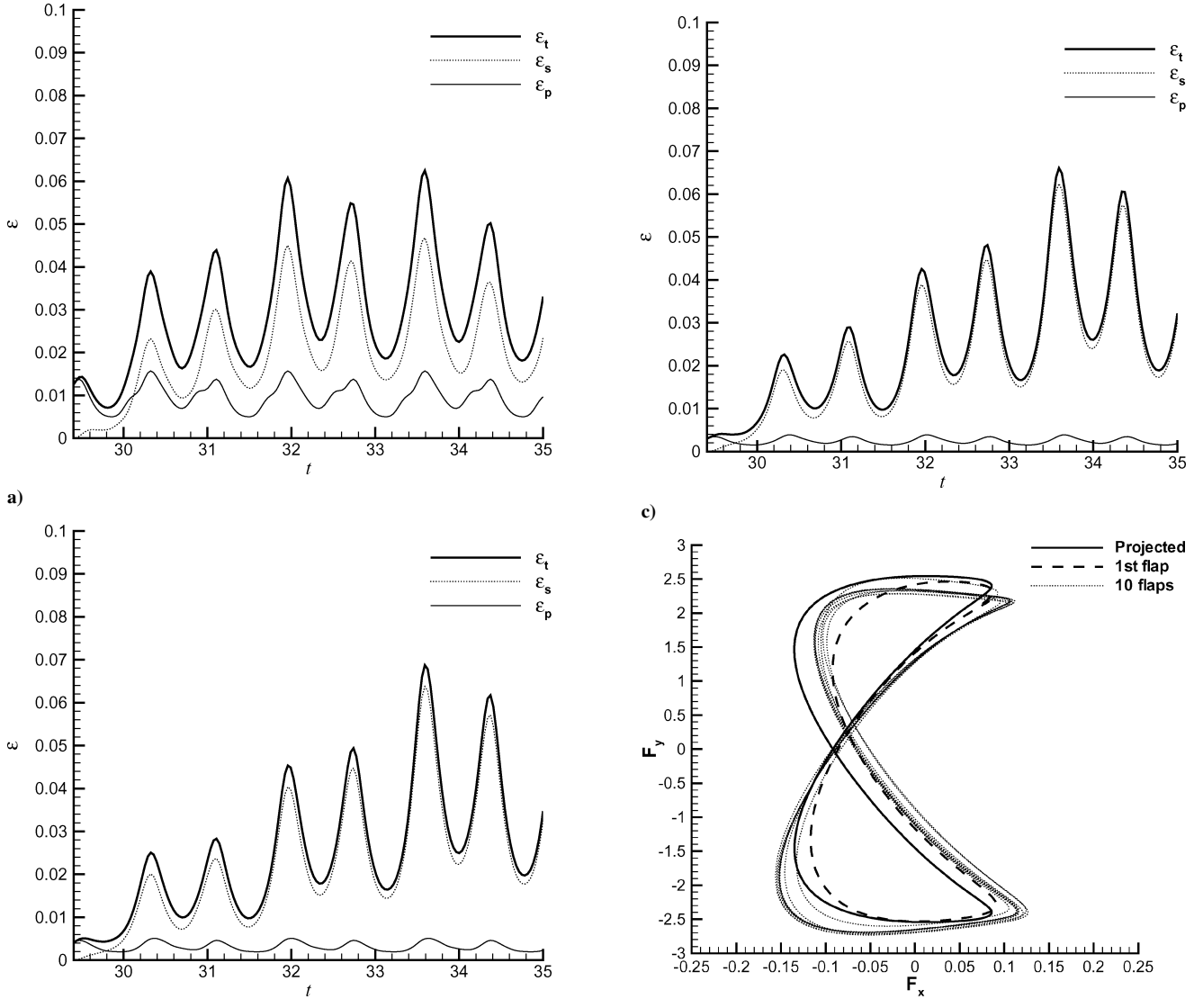

Fig. 10 Errors and force portraits for a reduced-order simulation with $k = 3.85$, $h = 0.2$ using a combined mode set generated from CFD simulations with $k = 3.57$, $h = 0.2$ and $k = 4.17$, $h = 0.2$: a) errors using nine modes ($\lambda_J/\lambda_1 \approx 10^{-2}$); b) errors using 18 modes ($\lambda_J/\lambda_1 \approx 10^{-3}$); c) errors using 26 modes ($\lambda_J/\lambda_1 \approx 10^{-4}$); and d) force portrait using 26 modes.

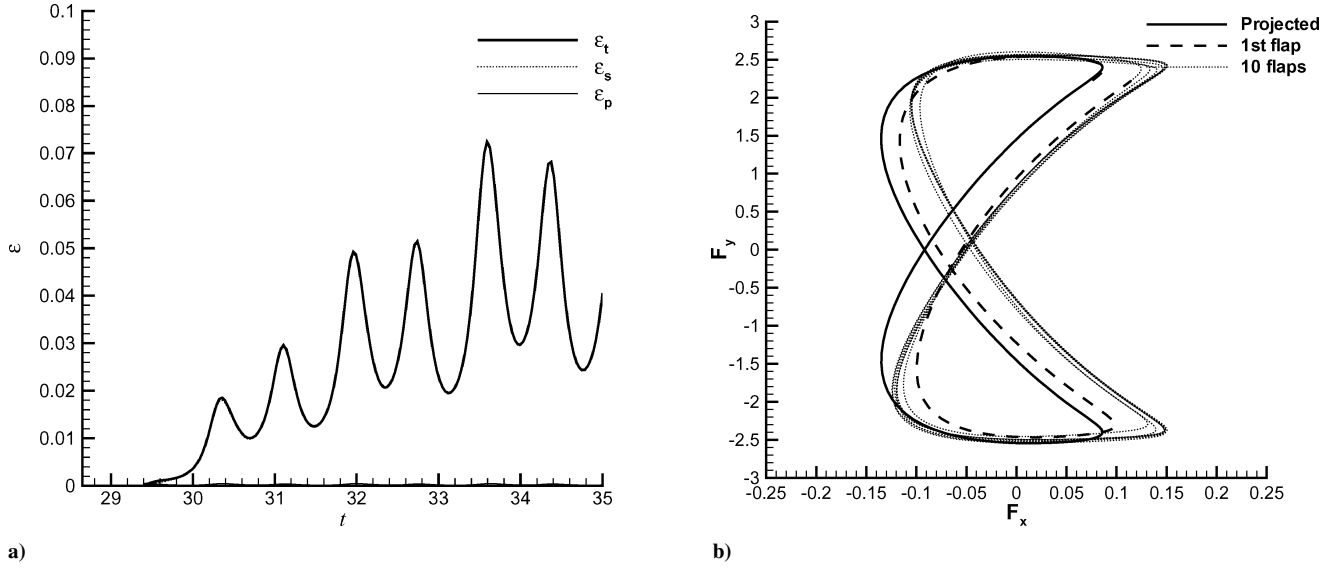

Fig. 11 Reduced-order simulation of a) errors and b) force portraits with $k = 3.85$, $h = 0.2$ using a combined mode set generated from CFD simulations with $k = 3.70$, $h = 0.2$ and $k = 4.00$, $h = 0.2$. Twenty-four POD modes were retained in the simulation ($\lambda_J/\lambda_1 \approx 10^{-4}$).

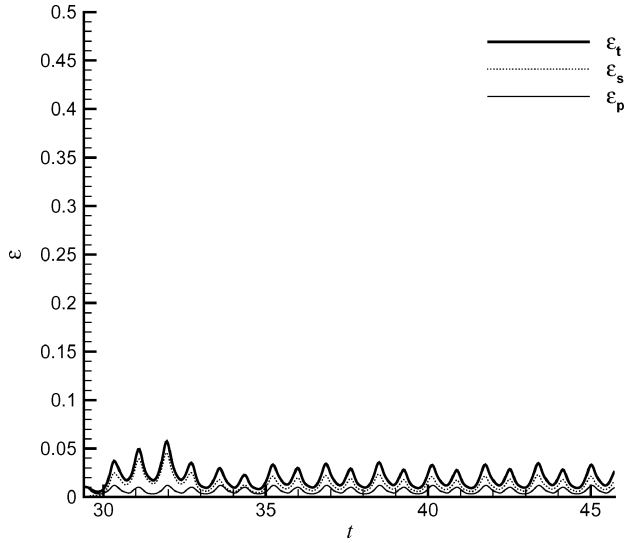

a)

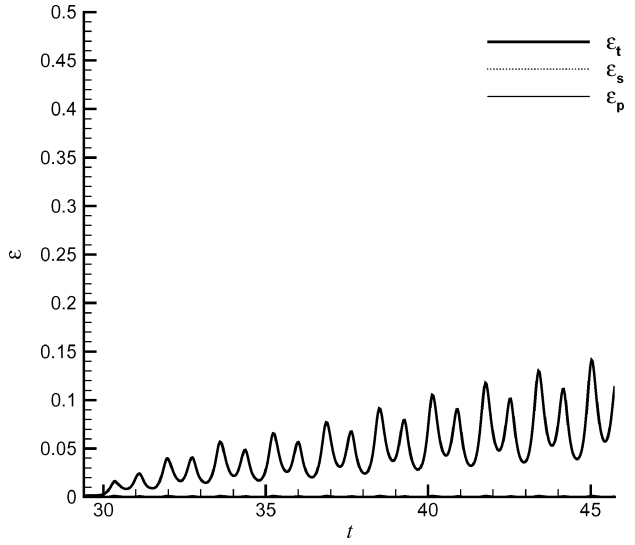

b)

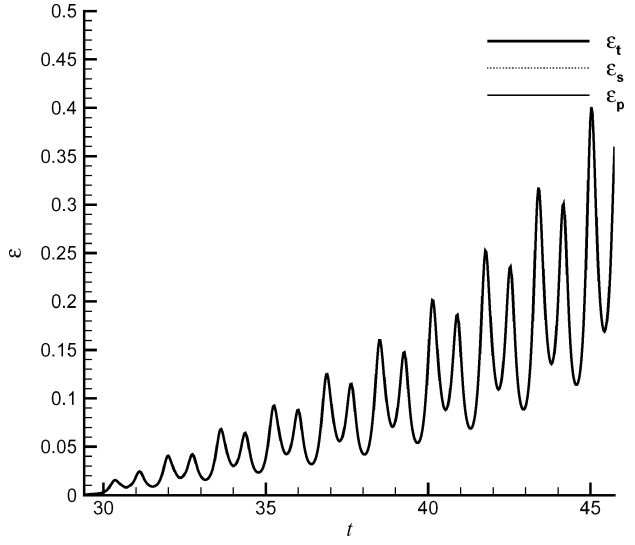

c)

Fig. 12 Projection, simulation, and total errors for a reduced-order simulation with $k = 3.85$, $h = 0.2$ using a combined mode set generated from CFD simulations with $k = 3.85$, $h = 0.1875$ and $k = 3.85$, $h = 0.2125$: a) seven modes ($\lambda_J/\lambda_1 \approx 10^{-2}$); b) 14 modes ($\lambda_J/\lambda_1 \approx 10^{-3}$); and c) 23 modes ($\lambda_J/\lambda_1 \approx 10^{-4}$).

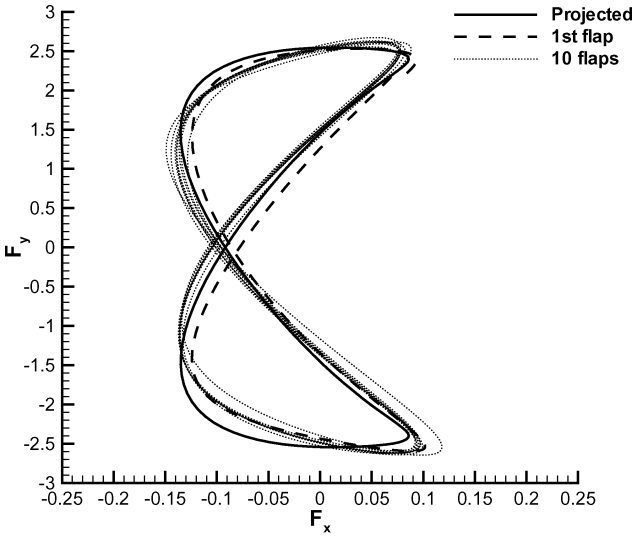

a)

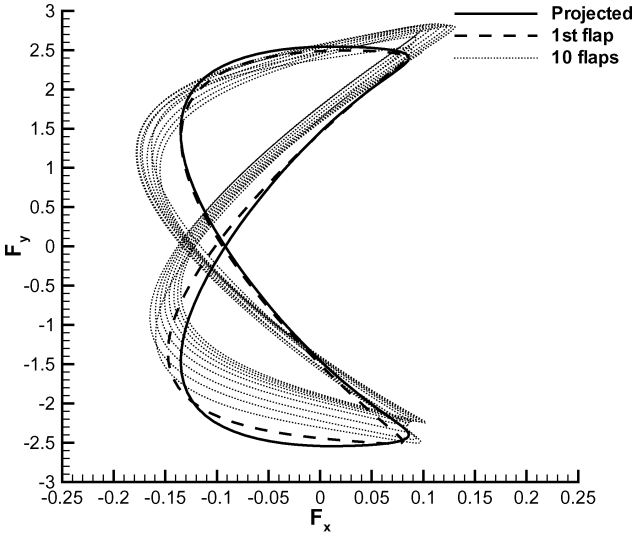

b)

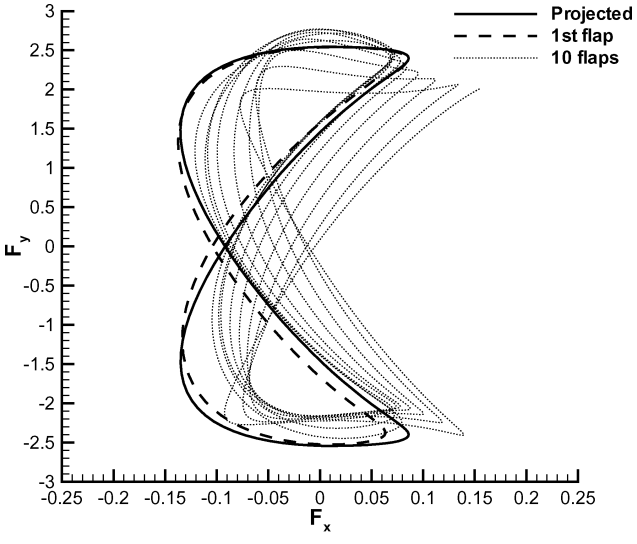

c)

Fig. 13 Force portraits for a reduced-order simulation with $k = 3.85$, $h = 0.2$ using a combined mode set generated from CFD simulations with $k = 3.85$, $h = 0.1875$ and $k = 3.85$, $h = 0.2125$: a) seven, b) 14, and c) 23 modes.

provide the ability to accurately simulate flows over a continuous, but small, frequency range ($\Delta k \approx 0.3$).

Variations in Amplitude

Similar analyses with variations in heaving amplitude show that retaining more modes in the simulations can result in very large long-term errors. For example, Fig. 12 shows the long-term errors for a reduced-order simulation with $k = 3.85$, $h = 0.2$ using modes generated from CFD results at $k = 3.85$, $h = 0.1875$ and $k = 3.85$, $h = 0.2125$ ($\Delta h = 0.025$). Note that when seven modes are retained, the projection errors are larger (as expected), but the long-term errors are substantially less than when 14 or 23 modes are retained. However, in the short term (i.e., on the order of one flap) the total errors are smaller when more modes are retained.

Analysis of the mode set suggests that the fine spatial structures in the lower energy modes are responsible for this phenomenon. Although the amplitudes are small, the product of the gradients [used to calculate the reduced-order model coefficients in Eq. (8)] can be quite large. In fact, the term $\nabla\mathbf{\Phi}_i \cdot \nabla\mathbf{\Phi}_i/\lambda_i$ is relatively constant for any given mode $\mathbf{\Phi}_i$. It is hypothesized that the dynamics of the lower energy modes cannot be fully captured because the temporal scale of their dynamics is smaller than that of the snapshots, allowing small errors in their coefficients to grow substantially over time. Although this phenomenon is present in many reduced-order simulations, it does not appear in all simulations, at least to the extent shown here. In particular, several simulations where k is varied do not exhibit this apparent instability with additional modes.

The errors in the reduced-order model coefficients are reflected in the force portraits for each simulation (Fig. 13). When 23 modes are retained, the forces track the CFD simulation very well for a substantial proportion of the first flap, although after several flaps the forces deviate considerably. Conversely, using only seven modes, the forces deviate by several percent even at the initiation of the simulation, but the long-term difference does not substantially increase, even after 10 flaps.

Note that the short-term errors for a narrow frequency range of $\Delta k/k \approx 7.8\%$ (Fig. 11) are comparable to the case immediately preceding (where the amplitude range is $\Delta h/h = 12.5\%$), whereas the forces are noticeably better in the latter (varying amplitude) case. Comparable errors were found for $\Delta k/k \approx 16\%$ and $\Delta h/h = 25\%$ (not shown), again indicating that the short-term simulation errors are more sensitive to variations in frequency than amplitude.

Extending the Parameter Range

The results of the preceding section show that small variations in heaving parameters can be accommodated by using mode sets generated by combining snapshots from pairs of CFD simulations. To be useful for control, however, the model must be able to simulate a much broader range of the parameter space. One straightforward method would be to have a number of POD mode sets (each generated from pairs of CFD simulations) and switch among them as the parameters of the flight regime change.

Alternatively, the POD modes can be enriched by including snapshots from additional CFD simulations. For example, snapshots from four simulations with varying frequency ($k = 3.45$, $k = 3.70$, $k = 4.00$, $k = 4.35$; all at $h = 0.2$) were combined to make one POD mode set, which was used to simulate heaving at three frequencies: $k = 3.57$, $k = 3.85$, and $k = 4.17$ (also at $h = 0.2$). Figures 14a–14c show the force portraits for each simulation. Figures 14d–14f show the results of simulations at the same frequencies using POD mode sets created from the nearest two sets of snapshots for each simulation. The number of modes retained in each simulation was adjusted until the results were of comparable accuracy for each frequency.

For similar results, 31 modes were needed for the large POD mode set, whereas only 11 modes were needed for each of the others. Thus, there is a tradeoff between the richness of the information contained in a mode set (and its corresponding ability to simulate a wide range of flow parameters) and the number of modes needed to maintain accuracy. Further, the increased information contained in the large mode set simplifies the controller logic in that no choice of mode

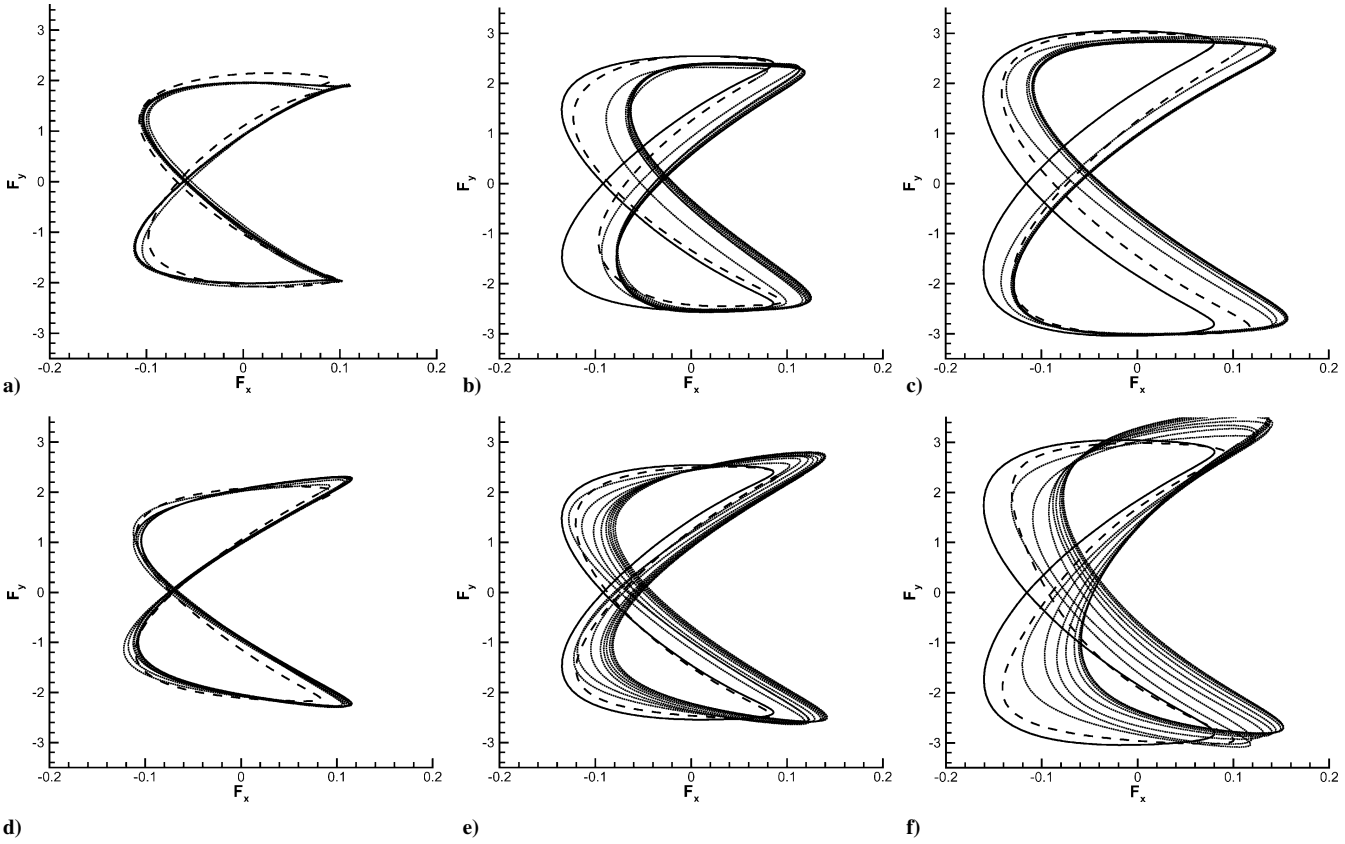

Fig. 14 Force portraits for several reduced-order simulations of varying frequency and $h = 0.2$: a) $k = 3.57$, b) $k = 3.85$, and c) $k = 4.17$ using 31 modes from a single POD mode set created from four sets of snapshots; d) $k = 3.57$, e) $k = 3.85$, and f) $k = 4.17$ using 11 modes created from two sets of snapshots.

set is needed. However, using the large mode set increases the operation count of the simulation because more modes are needed. The choice of models depends on the balance among logical complexity, computational complexity, and memory limitations.

Higher Energy Simulations

The simulations in the preceding section were performed at $k = 3.85$, $h = 0.2$. At $kh = 0.77$, this is a fairly unenergetic heaving mode compared to those for peak efficiency and power generation.[6] Simulations were also performed for heaving parameters centered about $k = 4.17$, $h = 0.25$. At $kh \approx 1.04$, the heaving parameters are much nearer those for maximum efficiency.

The results for these parameters are similar to those found in the preceding section. Figures 15 and 16 show the force portraits for mode sets created from combinations of snapshots that varied in both frequency (Fig. 15) and amplitude (Fig. 16). In each case, 24–26 modes are used in the reduced-order simulation, corresponding to $\lambda_J/\lambda_1 \approx 10^{-4}$. Note that forces are about as sensitive to changes in both frequency and heave amplitude as in the preceding section.

In particular, the deviation in the simulated forces when $\Delta k/k \approx 8\%$ (Fig. 15a) is comparable to the lower energy case with a similar variation in k (see Fig. 11b), whereas the forces for the

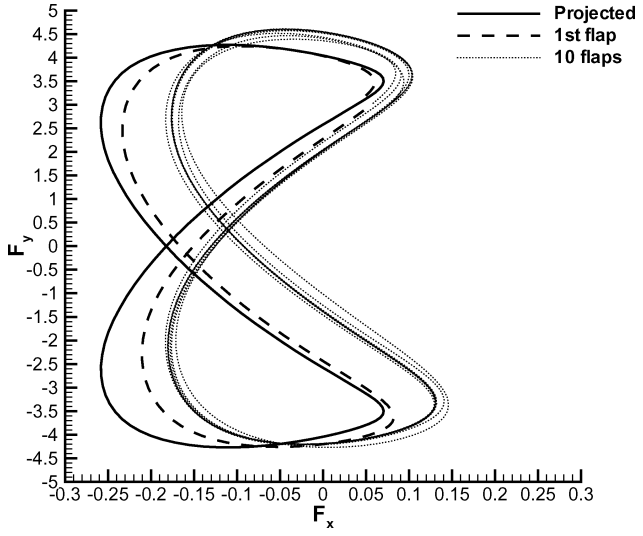

a)

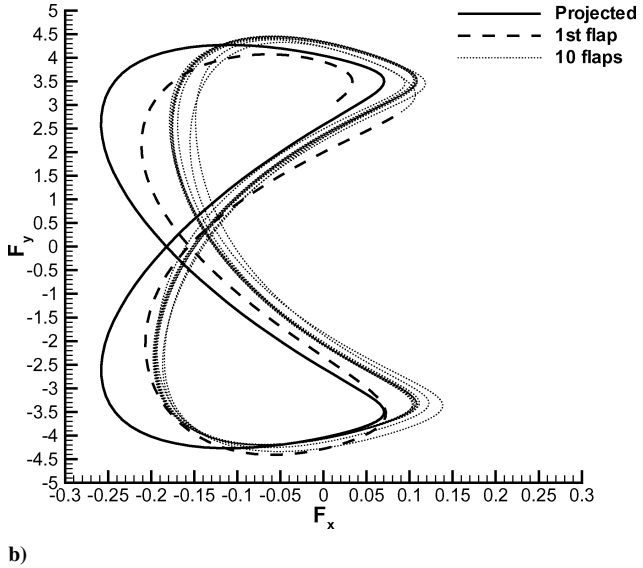

b)

Fig. 15 Force portraits for reduced-order simulations at $k = 4.17$, $h = 0.25$ using combined mode sets generated from CFD simulations with a) $k = 4.0$, $h = 0.25$ and $k = 4.35$, $h = 0.25$; and b) $k = 3.85$, $h = 0.25$ and $k = 4.55$, $h = 0.25$.

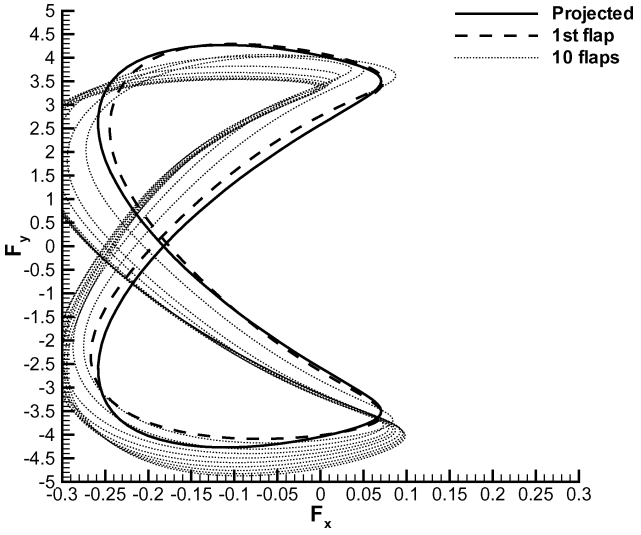

a)

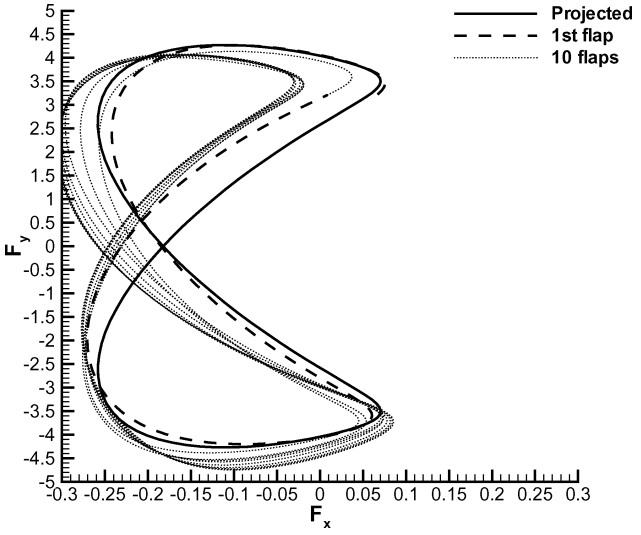

b)

Fig. 16 Force portraits for reduced-order simulations at $k = 4.17$, $h = 0.25$ using a combined mode sets generated from CFD simulations with a) $k = 4.17$, $h = 0.2375$ and $k = 4.17$, $h = 0.2625$; and b) $k = 4.17$, $h = 0.225$ and $k = 4.17$, $h = 0.275$.

case with $\Delta k/k \approx 17\%$ (Fig. 15b) deviate substantially. Also, the simulated forces for $\Delta h/h \approx 10\%$ (Fig. 16a) are excellent, whereas those for $\Delta h/h \approx 20\%$ (Fig. 16b) are still reasonable. Thus, it is expected that, at least for the periodic and symmetric region of the parameter space, the sensitivity of the reduced-order simulations to changes in k and h is similar to that presented earlier.

Conclusions

We have presented a reduced-order model based on proper orthogonal decomposition (POD) and a Galerkin projection for simulating the fluid dynamics around a flapping wing. The model accommodates variations in flapping parameters, but the parameter range within which reasonable results can be obtained is dependent on the method used to construct the POD mode sets.

Mode sets created from individual computational-fluid-dynamics (CFD) simulations are not useful for variations in flapping parameters. By combining snapshots from multiple CFD simulations, however, the reduced-order simulations can provide reliable results for small and moderate variations in flapping parameters. The results demonstrate the compromises between logical and computational complexity needed to extend the parameter range of the model. Specifically, to simulate larger changes in flapping parameters, two

alternatives are possible: 1) use many POD mode sets, each created from relatively few CFD simulations with narrow parameter ranges, and switch among the sets as necessary; or 2) generate one large mode set with a wide range of parameters from numerous CFD simulations. The former requires the parameter space to be "tiled," with the controller finding the best set of POD modes based on the current flapping parameters. This approach has the advantage of requiring smaller mode sets for any given set of parameters and is less computationally intensive. However, the latter approach is logically simpler in that only a single mode set is needed to cover the same parameter space; however, the number of modes needed to maintain accuracy is substantially increased, making this method more computationally intensive. Incidentally, the total number of modes in each of the cases is nearly identical (three sets of 11 modes for the former and one set of 31 modes for the latter).

Although the overall error of the reduced-order simulations is small (the difference in energy between the projected and simulated flows is often less than 10%), for some simulations the forces deviate noticeably before the completion of one flap and become totally inaccurate after several flaps. The lack of accuracy in long-term prediction, however, is not insurmountable. Indeed, if only long-term solutions (i.e., over several flaps such that the flow reaches a periodic state) are required, much more efficient, if not as elegant, solutions are possible (most notably, a simple look-up table with flapping parameters as inputs and forces and moments as outputs).

For active control at timescales at or less than one flap, the long-term inaccuracy can be overcome, given a suitable a method for observing the flow and feeding it back into the controller; feedback loops are routinely used to account for the inability of a model to perfectly account for the physics of the controlled system. However, implementing a feedback loop for the approach described in this work is not trivial because the method relies on global observability. That is, the POD modes are created from (spatially) complete knowledge of the velocity field. In practice, information about the flow would be limited to local properties near the airfoil such as pressure, velocity, or shear, or integrated properties such as total forces on the airfoil. Thus, a feedback loop could not use global knowledge of the velocity field to recalibrate the reduced-order model coefficients [e.g., by using the projection in Eq. (3)]. Instead, the locally observable properties would have to be correlated to the individual POD modes. For example, surface-mounted sensors (such as trigger hairs) on a wing could be used to measure the vorticity at the airfoil. By knowing the airfoil vorticity associated with each POD mode, given enough readings, the control model could be reset to the true state.

Such a control strategy was proposed by Gillies[8] in studies of vortex suppression of wake instabilities behind a circular cylinder. There can be many unstable modes in the vortex wake of a bluff body; using a single sensor proved useful only for Reynolds numbers slightly above the critical Reynolds number for the formation of a Karman vortex street. For higher Reynolds numbers with multiple unstable modes, a multiple-sensor control strategy was adopted and provided for good suppression of instabilities in numerical simulations.

Acknowledgments

This research was funded in part by NASA Grant NAG-1-01120, the Virginia Space Grant Consortium, and the John H. and Dorothy W. Sidebottom and Carlos A. and Esther H. Farrar Fellowships from the University of Virginia.

References

[1]Ashley, S., "Palm-Size Spy Planes," *Mechanical Engineering*, Vol. 120, No. 2, 1998, pp. 74–78.

[2]Srygley, R. B., and Thomas, A. L. R., "Unconventional Lift-Generating Mechanisms in Free-Flying Butterflies," *Nature*, Vol. 420, No. 6916, 2002, pp. 660–664.

[3]Fry, S. N., Sayaman, R., and Dickinson, M. H., "The Aerodynamics of Free-Flight Maneuvers in Drosophila," *Science*, Vol. 300, No. 5618, 2003, pp. 495–498.

[4]Gustafson, K., and Leben, R. R., "Robust Multigrid Computation and Visualization of Separation and Vortex Evolution in Aerodynamics Flows," *Proceedings of the 1st National Fluid Dynamics Congress*, AIAA, Washington, DC, 1988, pp. 174–184.

[5]Wang, Z. J., "Vortex Shedding and Frequency Selection in Flapping Flight," *Journal of Fluid Mechanics*, Vol. 410, 2000, pp. 323–341.

[6]Lewin, G. C., and Haj-Hariri, H., "Modelling Thrust Generation of a Two-Dimensional Heaving Airfoil in a Viscous Flow," *Journal of Fluid Mechanics*, Vol. 492, 2003, pp. 339–362.

[7]Cazemier, W., Verstappen, R. W. C. P., and Veldman, A. E. P., "Proper Orthogonal Decomposition and Low-Dimensional Models for Driven Cavity Flows," *Physics of Fluids*, Vol. 10, No. 7, 1998, pp. 1685–1699.

[8]Gillies, E. A., "Low-Dimensional Control of the Circular Cylinder Wake," *Journal of Fluid Mechanics*, Vol. 371, 1998, pp. 157–178.

[9]Arian, E., Fahl, M., and Sachs, E. W., "Trust-Region Proper Orthogonal Decomposition for Flow Control," NASA CR-2000-210124, May 2000.

[10]Ahlman, D., Söderlund, F. A., Kurdila, J. J., and Shyy, W., "Proper Orthogonal Decomposition for Time-Dependent Lid-Driven Cavity Flows," *Numerical Heat Transfer B*, Vol. 42, No. 4, 2002, pp. 285–306.

[11]Deane, A. E., Kevrekidis, I. G., Karniadakis, G. E., and Orszag, S. A., "Low-Dimensional Models for Complex Geometry Flows: Application to Grooved Channels and Circular Cylinders," *Journal of Computational Physics*, Vol. 98, No. 1, 1992, pp. 108–118.

[12]Graham, W. R., Peraire, J., and Tang, K. Y., "Optimal Control of Vortex Shedding Using Low-Order Models. Part I—Open Loop Model Development," *International Journal for Numerical Methods in Engineering*, Vol. 44, No. 7, 1999, pp. 945–972.

[13]Graham, W. R., Peraire, J., and Tang, K. Y., "Optimal Control of Vortex Shedding Using Low-Order Models. Part II—Model-Based Control," *International Journal for Numerical Methods in Engineering*, Vol. 44, 1999, pp. 973–990.

[14]Ma, X., and Karniadakis, G. E., "A Low-Dimensional Model for Simulating Three-Dimensional Cylinder Flow," *Journal of Fluid Mechanics*, Vol. 458, 2002, pp. 181–190.

[15]Ly, H. V., and Tran, H. T., "Modeling and Control of Physical Processes Using Proper Orthogonal Decomposition," *Mathematical and Computer Modelling*, Vol. 33, No. 1–3, 2001, pp. 223–236.

[16]Holmes, P., Lumley, J. L., and Berkooz, G., *Turbulence, Coherent Structures, Dynamical Systems and Symmetry*, Cambridge Univ. Press, Cambridge, England, U.K., 1996.

[17]Jones, K. D., Dohring, C. M., and Platzer, M. F., "Experimental and Computational Investigation of the Knoller-Betz Effect," *AIAA Journal*, Vol. 37, No. 7, 1998, pp. 1240–1246.

C. Pierre
Associate Editor